Correlated Mott insulators in strong electric fields: Role of phonons in heat dissipation

T. M. Mazzocchi [ORCID],[*] P. Gazzaneo [ORCID], J. Lotze [ORCID], and E. Arrigoni [ORCID][†]

Institute of Theoretical and Computational Physics, Graz University of Technology, 8010 Graz, Austria

We study the spectral and transport properties of a Mott insulator driven by a static electric field into a nonequilibrium steady state. For the dissipation, we consider two mechanisms: wide band fermion reservoirs and phonons included within the Migdal approximation. The electron correlations are treated via nonequilibrium dynamical mean field theory with an impurity solver suitable for strong correlations. We find that dissipation via phonons is limited to restricted ranges of field values around Wannier-Stark resonances. To cover the full range of field strengths, we allow for a small coupling with fermionic baths, which stabilizes the solution. When considering both dissipation mechanisms, we find that phonons enhance the current for field strengths close to half of the gap while lowering it at the gap resonance as compared to the purely electronic dissipation used by Murakami and Werner [Murakami and Werner, Phys. Rev. B **98**, 075102 (2018)]. Once phonons are the *only* dissipation mechanism, the current in the metallic phase is almost one order of magnitude smaller than the typical values obtained by coupling to a fermionic bath. In this case, the transport regime is characterized by an accumulation of charge in the upper Hubbard band described by two effective chemical potentials.

I. INTRODUCTION

One of the puzzling properties of strongly correlated materials is the occurrence of resistive switching in the form of an electric field driven insulator-to-metal transition [1]. The physical mechanism(s) leading to such a process is, as of yet, debated. In particular, the two most established explanations rely on either a thermal- [2,3] or quantum-triggered [4] origin of such phenomena.

Another possible explanation advocates the formation of conducting filaments percolating through the material. Recent work employed effective-resistor models [1,5] or a nonhomogeneous mean field approach [6] to describe the formation of such filaments. It is beyond doubt that a comprehensive description of these phenomena requires a deeper understanding of the microscopic mechanism behind the Joule heat transport.

However, beyond the relevance of the resistive switching transition, the problem of nonequilibrium transport of correlated electrons in a strong dc electric field and the occurrence of current-carrying regimes has attracted considerable attention in recent years [7–18]. As already pointed out in previous works [6,12–15,18–21], in order for the system to reach a nonequilibrium steady state, the current-induced Joule heat must be carried away. An efficient way to achieve this consists in the inclusion of fermionic reservoirs [2,3,14,18,19], also known as *Büttiker probes*. Their bandwidth is usually chosen to be large enough to ensure dissipation over the whole energy window of interest. Even though fermionic reservoirs proved themselves to be particularly well suited for the system to reach a stable, nontrivial steady-state solution [13,22], they

fail to capture the physical mechanism of heat transport mediated by lattice vibrations. An important step in this direction can be found in [4] where both phonons—connected to a bosonic bath—and fermionic reservoirs are included in two-dimensional Hubbard-like systems subject to a static field.

A description of the electric field driven insulator-to-metal transition is beyond the purpose of the present paper. We rather aim to model the heat dissipation of a Mott insulating system on a more realistic level by explicitly incorporating electron-phonon (e-ph) scattering as a dissipation channel. Similarly to [18], we focus on the Hubbard model within the dynamical mean field theory (DMFT) approximation. We find that the nonequilibrium picture near the current-carrying regions is significantly affected because of the different nature of the e-ph screening compared to the action of the fermionic baths.

In particular, when only phonons contribute to dissipation, their relatively narrow bandwidth makes it difficult to reach a stable steady-state [23] solution except for applied fields close to half of the band gap or the full band gap. Because of this limitation, addressing a wide region of field strengths requires coupling to a fermionic bath. We realize this mixed situation by weakly coupling to a fermionic Büttiker-like reservoir in addition to the phonons. Electronic correlations in this Hubbard model plus phonons are treated within DMFT using the auxiliary master equation approach (AMEA) impurity solver [24–28], which is particularly suited to treat strong correlations in a nonequilibrium steady state.

The results obtained in the mixed situation agree with [18] for both the spectral features and physical quantities. With respect to the previous work, we also study the dependence of the observables on the coupling to the fermionic bath. We find that phonons enhance the steady-state current for field strengths of the order of half of the gap while having no

*mazzocchi@tugraz.at
†arrigoni@tugraz.at

effect at the gap resonance, provided that the coupling to the fermionic bath is sufficiently small. We also show that phonons alone are far less effective as heat reservoirs, thus suppressing the current, especially at the full gap resonance.

This paper is organized as follows: In Sec. II we present the model Hamiltonian, while in Sec. III we briefly describe Floquet-DMFT (F-DMFT) [11,29,30] with the AMEA impurity solver. Our main results (Figs. 10 and 11) are discussed in Sec. IV, whereas Sec. V is left for final considerations.

II. MODEL HAMILTONIAN

Similarly to [18], we consider an extension of the Hubbard model in the presence of an electric field described by the Hamiltonian

$$\hat{H}(t) = \varepsilon_c \sum_{i\sigma} \hat{n}_{i\sigma} - \sum_{\sigma} \sum_{(i,j)} t_{ij}(t) \hat{c}_{i\sigma}^\dagger \hat{c}_{j\sigma} + U \sum_i \hat{n}_{i\uparrow} \hat{n}_{i\downarrow}$$
$$+ \hat{H}_{\text{bath}} + \hat{H}_{\text{e-ph}} + \hat{H}_{\text{ph}}. \quad (1)$$

The operator $\hat{c}_{i\sigma}^\dagger$ ($\hat{c}_{i\sigma}$) creates (annihilates) an electron of spin $\sigma = \{\uparrow, \downarrow\}$ at the ith lattice site, with the corresponding density operator $\hat{n}_{i\sigma} \equiv \hat{c}_{i\sigma}^\dagger \hat{c}_{i\sigma}$. Nearest neighbor sites are denoted by (i, j) and the electrons' *onsite energy* is $\varepsilon_c \equiv -U/2$. The static homogeneous electric field is introduced within the temporal gauge and enters in the time dependence of the hopping in Eq. (1) via the Peierls substitution [31]

$$t_{ij}(t) = t_c \, e^{-i\frac{q}{\hbar}(\boldsymbol{r}_j - \boldsymbol{r}_i) \cdot \boldsymbol{A}(t)}, \quad (2)$$

where t_c is the lattice hopping amplitude, $\boldsymbol{A}(t)$ is the vector potential, q is the electron charge, and $\hbar$ is Planck's constant. We choose the electric field $\boldsymbol{F} = -\partial_t \boldsymbol{A}(t)$ and thus $\boldsymbol{A}(t) = \boldsymbol{e}_0 A(t)$ to point along the lattice body diagonal, i.e., $\boldsymbol{e}_0 = (1, 1, \dots, 1)$, and work in the temporal gauge:

$$\boldsymbol{A}(t) = -\boldsymbol{F} \, t. \quad (3)$$

Equations (2) and (3) introduce the Bloch frequency $\Omega \equiv -Fqa/\hbar$, with a being the lattice spacing. In this paper we consider a d-dimensional lattice in the $d \to \infty$ limit [18] with the usual rescaling of the hopping $t_c = t^*/(2\sqrt{d})$. This way, sums over the crystal momentum $\sum_{\boldsymbol{k}} \chi(\omega, \boldsymbol{k})$ of generic quantities χ can be replaced by an integral [29] $\int d\epsilon \int d\bar{\epsilon} \, \rho(\epsilon, \bar{\epsilon}) \chi(\omega; \epsilon, \bar{\epsilon})$, where $\rho(\epsilon, \bar{\epsilon}) = 1/(\pi t^{*2}) \exp(-(\epsilon^2 + \bar{\epsilon}^2)/t^{*2})$ is the joint density of states (JDOS) and

$$\epsilon = -2t_c \sum_{i=1}^{d} \cos(k_i a),$$
$$\bar{\epsilon} = -2t_c \sum_{i=1}^{d} \sin(k_i a). \quad (4)$$

Electron-phonon coupling is included in the form of an acoustic phonon branch attached to each lattice site:

$$\hat{H}_{\text{e-ph}} = g \sum_i (\hat{n}_{i\uparrow} + \hat{n}_{i\downarrow}) \hat{x}_i, \quad (5)$$

where $\hat{x}_i \equiv (\hat{b}_i^\dagger + \hat{b}_i)/\sqrt{2}$ and $\hat{b}_i^\dagger$ ($\hat{b}_i$) creates (annihilates) a phonon belonging to the branch i. We include the dispersion of each branch in $\hat{H}_{\text{ph}}$, which will be discussed in Sec. III B [32].

As pointed out in the introduction, a stable steady state is difficult to achieve when considering dissipation by phonons only. Due to the narrow phonon dispersion, multiphonon processes would be necessary in order to relax electrons across the Hubbard gap. For this reason, we additionally include fermionic baths and try to extrapolate the properties of the system to the limit where the coupling to these baths becomes negligible. The fermionic baths are in the form of *infinite* tight-binding chains attached to each lattice site [6,20,21,33]. The corresponding Hamiltonian reads

$$\hat{H}_{\text{bath}} = -t_b \sum_{\alpha j\sigma} (\hat{f}_{\alpha j\sigma}^\dagger \hat{f}_{\alpha j+1\sigma} + \text{H.c.}) + \varepsilon_b \sum_{\alpha j\sigma} \hat{n}_{\alpha j\sigma}^f$$
$$= -v \sum_{j\sigma} (\hat{c}_{j\sigma}^\dagger \hat{f}_{1j\sigma} + \text{H.c.}), \quad (6)$$

where $\hat{f}_{\alpha j\sigma}^\dagger$ ($\hat{f}_{\alpha j\sigma}$) creates (annihilates) an electron with spin σ at position α along the jth bath chain and $\hat{n}_{\alpha j\sigma}^f$ is the corresponding density operator. The last term in Eq. (6) accounts for the hybridization between the jth site in the lattice and the corresponding bath chain. In this paper we set $\hbar = k_B = a = 1 = -q$, such that $\Omega \equiv F$, i.e., current and electric field are measured in units of t^*.

III. METHOD AND FORMALISM

A. Floquet Green's functions

Due to the periodicity of the nonequilibrium Green's functions (GFs) in the temporal gauge [34], $G(t, t') = G(t + \tau, t' + \tau)$ with $\tau = 2\pi/\Omega$, it is convenient to represent them in the *Keldysh-Floquet* formalism [11,29,30]

$$\underline{G}_{mn}(\omega) = \int dt_{\text{rel}} \int_{-\tau/2}^{\tau/2} \frac{dt_{\text{av}}}{\tau} e^{i[(\omega + m\Omega)t - (\omega + n\Omega)t']} \underline{G}(t, t') \quad (7)$$

with the *Wigner* GF [29]

$$\underline{G}_l(\omega) = \int dt_{\text{rel}} \int_{-\tau/2}^{\tau/2} \frac{dt_{\text{av}}}{\tau} e^{i\omega t_{\text{rel}} + il\Omega t_{\text{av}}} \underline{G}(t, t'). \quad (8)$$

As usual, $t_{\text{rel}} = t - t'$ and $t_{\text{av}} = (t + t')/2$ are the relative and average time variables. Equations (7) and (8) are connected via

$$\underline{G}_{mn}(\omega) = \underline{G}_{m-n}\left(\omega + \frac{m+n}{2}\Omega\right). \quad (9)$$

In this paper any Floquet-represented matrix is referred to as either X_{mn} explicitly showing its indices or a boldface letter $\boldsymbol{X}$. On the other hand, a single index as subscript X_l is reserved for the Wigner representation. Finally, an underline indicates the Keldysh structure

$$\underline{\boldsymbol{G}} \equiv \begin{pmatrix} \boldsymbol{G}^R & \boldsymbol{G}^K \\ \boldsymbol{0} & \boldsymbol{G}^A \end{pmatrix}, \quad (10)$$

which contains the *retarded*, *advanced*, and *Keldysh* components $\boldsymbol{G}^{R,A,K}$, where $\boldsymbol{G}^A = (\boldsymbol{G}^R)^\dagger$. It is worth recalling the definition $\boldsymbol{G}^K \equiv \boldsymbol{G}^> + \boldsymbol{G}^<$, with $\boldsymbol{G}^{\lessgtr}$ denoting the *lesser* and *greater* components [35–38].

B. Dyson equation

The lattice Floquet GF obeys the Dyson equation

$$\underline{\boldsymbol{G}}^{-1}(\omega, \epsilon, \overline{\epsilon}) = \underline{\boldsymbol{G}}_0^{-1}(\omega, \epsilon, \overline{\epsilon}) - \underline{\boldsymbol{\Sigma}}(\omega, \epsilon, \overline{\epsilon}) - \underline{\boldsymbol{\Sigma}}_{\text{e-ph}}(\omega, \epsilon, \overline{\epsilon}) \tag{11}$$

with both electron and e-ph self-energies (SEs) depending on the crystal momentum via ϵ and $\overline{\epsilon}$. The lattice GF of the noninteracting part of the Hamiltonian (1) reads

$$\underline{G}_{0,mn}^{-1}(\omega, \epsilon, \overline{\epsilon}) = \underline{g}_{0,mn}^{-1}(\omega, \epsilon, \overline{\epsilon}) - \delta_{mn}\, v^2 \underline{g}_{\text{bath}}(\omega + n\Omega) \tag{12}$$

with

$$\begin{aligned}
\left[g_0^{-1}(\omega, \epsilon, \overline{\epsilon}) \right]_{mn}^{\text{R}} &= (\omega + n\Omega + i0^+ - \varepsilon_c)\delta_{mn} - \varepsilon_{mn}(\epsilon, \overline{\epsilon}), \\
\left[g_0^{-1}(\omega, \epsilon, \overline{\epsilon}) \right]_{mn}^{\text{K}} &\to 0.
\end{aligned} \tag{13}$$

The inverse Keldysh component is negligible in comparison with $\text{Im}(g_{\text{bath}}^{\text{K}})$ since it is proportional to an imaginary infinitesimum. The Floquet dispersion relation ε_{mn} for a dc field in a hypercubic lattice [29] is given by

$$\varepsilon_{mn}(\epsilon, \overline{\epsilon}) = \tfrac{1}{2}[(\epsilon + i\overline{\epsilon})\delta_{m-n,1} + (\epsilon - i\overline{\epsilon})\delta_{m-n,-1}]. \tag{14}$$

In the wide band limit considered here, the *retarded* and *Keldysh* components of the electronic bath's GF (12) [33] read

$$\begin{aligned}
v^2 g_{\text{bath}}^{\text{R}}(\omega) &= -\frac{i}{2}\, \Gamma_{\text{e}}, \\
v^2 g_{\text{bath}}^{\text{K}}(\omega) &= -i\, \Gamma_{\text{e}}\, \tanh\left[\frac{\beta}{2}(\omega - \mu) \right],
\end{aligned} \tag{15}$$

where the *Keldysh* component is obtained from the *fluctuation-dissipation* theorem $g_{\text{bath}}^{\text{K}}(\omega) = [g_{\text{bath}}^{\text{R}}(\omega) - g_{\text{bath}}^{\text{A}}(\omega)] \tanh[\beta(\omega - \mu)/2]$. In Eq. (15), μ denotes the chemical potential, while $\beta \equiv 1/T$ is the inverse temperature and Γ_{e} is the coupling strength to the fermionic reservoir. The electron SE $\underline{\boldsymbol{\Sigma}}$ is obtained from F-DMFT the only approximation of which consists in neglecting its crystal momentum dependence $\underline{\boldsymbol{\Sigma}}(\omega, \epsilon, \overline{\epsilon}) \approx \underline{\boldsymbol{\Sigma}}(\omega)$. Further details will be given in Sec. III C.

1. Implementation of the electron-phonon SE

Within the F-DMFT approximation, the e-ph SE is also included as a local contribution $\underline{\boldsymbol{\Sigma}}_{\text{e-ph}}(\omega, \epsilon, \overline{\epsilon}) \approx \underline{\boldsymbol{\Sigma}}_{\text{e-ph}}(\omega)$. In terms of the contour time arguments z and z' it has the form

$$\Sigma_{\text{e-ph}}(z, z') = ig^2 G(z, z') D_{\text{ph}}(z, z') \tag{16}$$

corresponding to the lowest-order diagram in the bare phonon propagator D_{ph}. The explicit form of the retarded and Keldysh components associated with Eq. (16) can be found in Appendix B. In Eq. (16), $G(z, z')$ is the local electron Green's function, the Keldysh-Floquet representation of which is obtained as

$$\begin{aligned}
\underline{\boldsymbol{G}}_{\text{loc}}(\omega) = &\int d\epsilon \int d\overline{\epsilon}\, \rho(\epsilon, \overline{\epsilon}) \\
&\times \left\{ \left[\underline{\boldsymbol{G}}_0^{-1}(\omega, \epsilon, \overline{\epsilon}) - \underline{\boldsymbol{\Sigma}}(\omega) - \underline{\boldsymbol{\Sigma}}_{\text{e-ph}}(\omega) \right]^{-1} \right\}. \tag{17}
\end{aligned}$$

Due to gauge invariance, $\underline{\boldsymbol{G}}_{\text{loc}}(\omega)$ is diagonal in Floquet indices in the case of a dc field [29]. The Keldysh components

[39] of $D_{\text{ph}}(z, z')$ at equilibrium [40] are given by

$$\begin{aligned}
D_{\text{ph}}^{\text{R}}(t, t') &= -i\theta(t - t') \int d\omega\, e^{-i\omega(t-t')} A_{\text{ph}}(\omega), \\
D_{\text{ph}}^{>}(t, t') &= -i \int d\omega\, e^{-i\omega(t-t')} A_{\text{ph}}(\omega)[1 + b(\omega)] \\
D_{\text{ph}}^{<}(t, t') &= -i \int d\omega\, e^{-i\omega(t-t')} A_{\text{ph}}(\omega)\, b(\omega),
\end{aligned} \tag{18}$$

where $b(\omega) = 1/(e^{\beta\omega} - 1)$ is the Bose-Einstein distribution function at inverse temperature β. We focus on acoustic phonons, with spectral function $A_{\text{ph}}(\omega) = \omega/(4\omega_{\text{ph}}^2)e^{-|\omega|/\omega_{\text{ph}}}$, ω_{ph} being a soft cutoff frequency [41]. Details about the explicit form of the phonon spectral function can be found in Appendix C.

C. Floquet DMFT

The electron SE in Eq. (11) is determined within the DMFT approach [42–44], and in particular its nonequilibrium Floquet (F-DMFT) extension [11,29,30]. This consists in neglecting the crystal momentum dependence of the electron SE, i.e., $\underline{\boldsymbol{\Sigma}}(\omega, \epsilon, \overline{\epsilon}) \to \underline{\boldsymbol{\Sigma}}(\omega)$. This reduces to mapping the original problem onto a single-site impurity model—the GF $\underline{g}_{0,\text{site}}^{-1}(\omega)$ of which is defined as in Eq. (13) by replacing $\varepsilon_{mn}(\epsilon, \overline{\epsilon}) \to \varepsilon_{\text{c}}$—encoding the effect of all other lattice sites into an *effective* bath hybridization function, $\underline{\boldsymbol{\Delta}}(\omega)$.

The GF of the resulting impurity model must be determined by a many-body impurity solver, in this case a nonequilibrium one, which constitutes the bottleneck of the approach. The hybridization $\underline{\boldsymbol{\Delta}}(\omega)$ is fixed by the condition that the local and impurity GFs coincide, i.e., $\underline{\boldsymbol{G}}_{\text{imp}}(\omega) \overset{!}{=} \underline{\boldsymbol{G}}_{\text{loc}}(\omega)$. In practice, this self-consistency condition is carried out by (i) starting from a guess for the two SEs $\underline{\boldsymbol{\Sigma}}(\omega)$ and $\underline{\boldsymbol{\Sigma}}_{\text{e-ph}}(\omega)$, (ii) computing the GF and obtaining $\underline{\boldsymbol{G}}_{\text{loc}}(\omega)$ following Eq. (17), (iii) computing $\underline{\boldsymbol{\Sigma}}_{\text{e-ph}}(\omega)$ from (16) (see also Appendix B), (iv) extracting $\underline{\boldsymbol{\Delta}}(\omega)$ from

$$\underline{\boldsymbol{G}}_{\text{loc}}^{-1}(\omega) = \underline{g}_{0,\text{site}}^{-1}(\omega) - \underline{\boldsymbol{\Delta}}(\omega) - \underline{\boldsymbol{\Sigma}}(\omega), \tag{19}$$

(v) solving the many-body impurity problem and determining the new $\underline{\boldsymbol{\Sigma}}(\omega)$, and (vi) using the obtained SEs in step (ii). Steps (ii)–(v) are then iterated until convergence.

Notice that, for the same reason as for the local Green's function, also $\underline{\boldsymbol{\Delta}}(\omega)$, $\underline{\boldsymbol{\Sigma}}(\omega)$, and $\underline{\boldsymbol{\Sigma}}_{\text{e-ph}}(\omega)$ are diagonal in Floquet indices. This, combined with the translation property $\underline{G}_{mm}(\omega) = \underline{G}_{00}(\omega + m\Omega)$ following Eq. (7) and being valid for the above quantities as well, allows us to restrict the problem to the $(0,0)$ element only.

1. Auxiliary master equation approach

As mentioned above, the most difficult part of the DMFT algorithm is the solution of the impurity problem. At the moment, in contrast to equilibrium there is no well established impurity solver for the nonequilibrium case [39]. The AMEA [24–26,45] adopted here maps the impurity problem, the bath hybridization function of which is defined as in

Eq. (19), onto an *auxiliary* open quantum system consisting of a finite number of bath sites N_B attached to Markovian reservoirs described by the Lindblad equation. Its corresponding noninteracting hybridization function $\underline{\Delta}_{aux}(\omega)$ is obtained by fitting the original interacting DMFT one. Convergence is reached once $\underline{\Delta}_{aux}$ agrees with $\underline{\Delta}$ with sufficient accuracy. With the system parameters obtained from $\underline{\Delta}_{aux}$, the auxiliary problem can then be solved exactly by many-body-diagonalization methods for open quantum systems yielding the required impurity Green's function. The convergence of AMEA increases exponentially with the number of bath sites N_B [45]. To speed up the whole process, it turns out convenient to first solve the auxiliary impurity problem with $N_B = 4$ to get suitable initial SEs to be provided as an input for the simulations with $N_B = 6$. [46]

D. Physical quantities

The local electronic spectral function is given by

$$A(\omega) = -\frac{1}{\pi}\text{Im}\big[G_{\text{loc}}^{R}(\omega)\big], \tag{20}$$

where G_{loc}^{R} is the *retarded* component of the GF given in Eq. (17).

The nonequilibrium distribution function

$$F_{\text{neq}}(\omega) = \frac{1}{2}\left\{1 - \frac{1}{2}\frac{\text{Im}\big[G_{\text{loc}}^{K}(\omega)\big]}{\text{Im}\big[G_{\text{loc}}^{R}(\omega)\big]}\right\} \tag{21}$$

is related to the electronic spectral occupation function via

$$N_e(\omega) \equiv A(\omega)F_{\text{neq}}(\omega). \tag{22}$$

In our units, the time-resolved current $j(t)$ and kinetic energy $E_{\text{kin}}(t)$ are given by

$$j(t) = 2i\sum_{\mathbf{k}}[\mathbf{e}_0 \cdot \mathbf{v}_{\mathbf{k}}(t)]G_{\mathbf{k}}^{<}(t,t), \tag{23}$$

$$E_{\text{kin}}(t) = -2i\sum_{\mathbf{k}}\varepsilon_{\mathbf{k}}(t)G_{\mathbf{k}}^{<}(t,t), \tag{24}$$

where the group velocity $\mathbf{v}_{\mathbf{k}}(t) = \nabla_{\mathbf{k}}\varepsilon_{\mathbf{k}}(t)$ is obtained from the dispersion relation $\varepsilon_{\mathbf{k}}(t) = \epsilon \cos[A(t)] + \bar{\epsilon}\sin[A(t)]$ following from Eqs. (4) and (14), while the factor 2 accounts for spin degeneracy. The Wigner-represented current is given by

$$j_l = \int_{-\infty}^{+\infty}\frac{d\omega}{2\pi}\, j_l(\omega) \tag{25}$$

with the frequency-resolved current

$$j_l(\omega) = \int d\epsilon \int d\bar{\epsilon}\, \rho(\epsilon,\bar{\epsilon})[(\epsilon - i\bar{\epsilon})G_{l+1}^{<}(\omega,\epsilon,\bar{\epsilon}) + \text{H.c.}]. \tag{26}$$

The Wigner-represented kinetic energy is

$$E_{\text{kin},l} = \int_{-\infty}^{+\infty}\frac{d\omega}{2\pi}\, E_{\text{kin},l}(\omega) \tag{27}$$

with the frequency-resolved kinetic energy

$$E_{\text{kin},l}(\omega) = \int d\epsilon \int d\bar{\epsilon}\, \rho(\epsilon,\bar{\epsilon})$$
$$\times [-(\bar{\epsilon} + i\epsilon)G_{l+1}^{<}(\omega,\epsilon,\bar{\epsilon}) + \text{H.c.}]. \tag{28}$$

The explicit derivation of the expressions above is contained in Appendix A. Again, the $l \neq 0$ components of these quantities vanish by means of gauge invariance due to the time-independent nature of the dc field setup. For this reason, we will drop the index l from now on.

IV. RESULTS

Our aim is to study the effect of a strong dc electric field which is comparable to the gap in Mott insulators. Therefore we choose $U/t^* = 8$ for which the system shows a well established insulating phase [18]. All simulations are carried out at half filling with $\varepsilon_c = -U/2$, inverse temperature $\beta = 20/t^*$, and chemical potential $\mu = 0$. We define the phonon coupling strength [47] as

$$\Gamma_{\text{ph}} \equiv 2\pi g^2 A_{\text{ph}}(\omega_{\text{ph}}) = \frac{\pi}{2e}\left(\frac{g^2}{\omega_{\text{ph}}}\right), \tag{29}$$

which allows us to introduce the dimensionless electron-to-phonon ratio $\gamma \equiv \Gamma_e/\Gamma_{\text{ph}}$ as a measure of their relative strength, with Γ_e given in Eq. (15). In this paper, we focus on $\gamma \ll 1$ to keep the influence of the fermionic bath as small as possible [48]. We choose as default values $\Gamma_{\text{ph}}/t^* = 0.925$ and $\omega_{\text{ph}}/t^* = 0.1$ if not stated otherwise.

As discussed above, phonons provide a valid dissipation channel with a stable steady state only around specific values of the electric field $\mathbf{F}$. To achieve numerical stability for a wide range of $\mathbf{F}$, we need to include a weakly coupled fermionic reservoir. In Sec. IV A, we then vary the coupling Γ_e with the fermionic bath in addition to dissipation via phonons. We discuss the case of purely phononic dissipation $\Gamma_e = 0$ [49] in Sec. IV B.

A. Phonons and electron baths

1. Spectral properties

In equilibrium at $F = 0$, the local spectral function $A(\omega)$ shown in Fig. 1(a) displays the spectrum of the Mott insulator weakly connected to a metallic bath which is characterized by the upper Hubbard band (UHB) and the lower Hubbard band (LHB) at $\omega_{\text{HB},\pm} \approx \pm U/2$ with bandwidths [50] of about $2t^*$.

In the regime of small electric fields, increasing the field raises the potential energy drop between neighboring sites, thus localizing the electrons further. The effect is clearly visible in Fig. 2(a), where the spectral weight is shifted from the main Hubbard bands to satellite peaks located at integer multiples [14] of the field F. The overall structure is known as the Wannier-Stark (WS) ladder in noninteracting systems [51,52] while in the context of many-body physics [18] it has been also referred to as the Bloch-Zener archipelago [14]. Injecting energy into the system via the applied field heats up the electrons, which results in a nonequilibrium distribution function characterized by a higher temperature as compared to the equilibrium case $F = 0$ [see Fig. 2(b)].

At larger fields as shown in Fig. 3 the in-gap WS satellite peaks $\omega_{\text{WS},\pm,\mp} = \pm(U/2) \mp F$ grow in magnitude [see
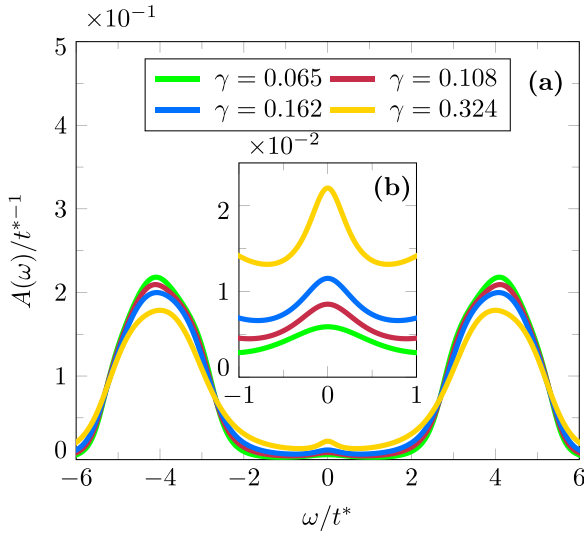
FIG. 1. (a) Spectral function $A(\omega)/t^{*-1}$ at zero electric field $F = 0$ for different values of the ratio γ. The inset (b) shows the magnified quasiparticle peak at $\omega = 0$. Default parameters are specified at the beginning of Sec. IV.

FIG. 3. Spectral function $A(\omega)/t^{*-1}$ (solid) and spectral occupation $N_e(\omega)/t^{*-1}$ (shaded area) at (a) $F = 3t^*$, (b) $F = 4t^*$, (c) $F = 5.6t^*$, and (d) $F = 8t^*$. Here $\gamma = 0.065$. Default parameters are specified at the beginning of Sec. IV.

Fig. 2(a)]. In this regime, increasing the field lets these peaks come closer until they overlap at $F \approx U/2$ as evidenced by Fig. 3(b). Exceeding $U/2$, the electric field pushes the WS peaks further towards the Hubbard bands at $\omega_{\mathrm{HB},\mp}$ as can be inferred from Fig. 3(c).

Altogether, the emergence of WS sidebands can be understood as the overlap between LHB and UHB of neighboring sites along the $\boldsymbol{e}_0$ direction of the electric field. Due to the field-induced potential drop, the Hubbard bands shift in opposite directions until field strengths of $F \approx U$ are reached where the LHB and UHB of neighboring sites overlap [see Fig. 3(d)]. The in-gap WS *islands* effectively lower the energy separation between the main Hubbard bands and facilitate the motion of electrons for $F < U$, as we will discuss in the following.

In Fig. 3(a), we observe that for $F = 3t^*$ the WS sidebands lie at $\omega_{\mathrm{WS},\pm,\mp} \approx \pm t^*$. Subject to the field, an electron within the LHB gains the energy to reach $\omega_{\mathrm{WS},-,+} \approx -t^*$. The corresponding spectral occupation $N_e(\omega)$ shows that this sideband is completely occupied. Due to the charge motion from the
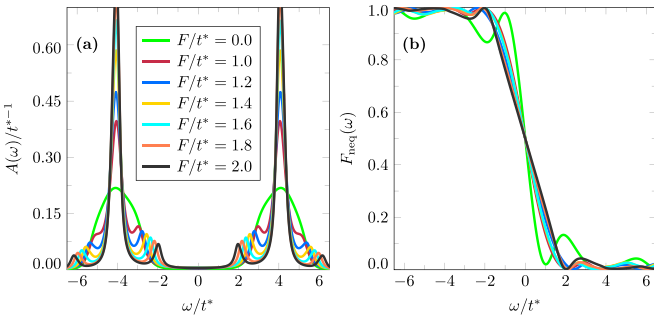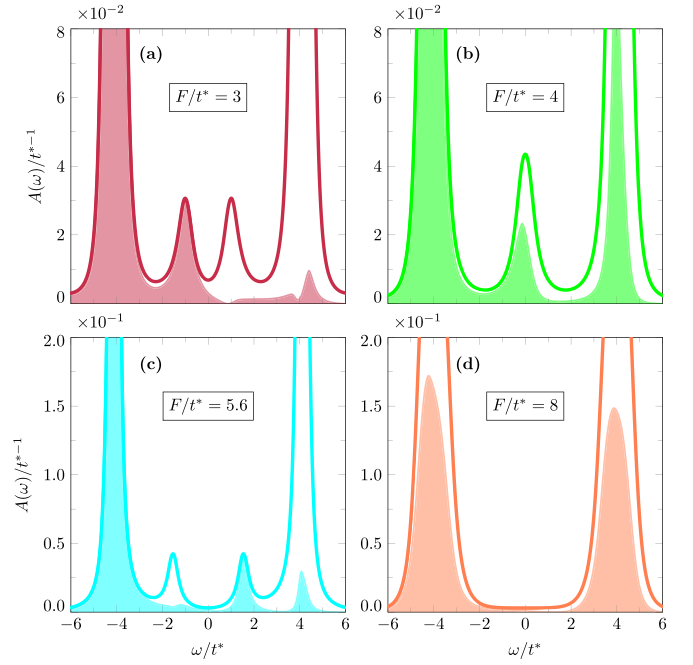

FIG. 2. (a) Spectral function $A(\omega)/t^{*-1}$ and (b) nonequilibrium distribution function $F_{\mathrm{neq}}(\omega)$ for various field strengths at $\gamma = 0.065$. Default parameters are specified at the beginning of Sec. IV.

LHB to $\omega_{\mathrm{WS},-,+} \approx -t^*$, we expect the current to be slightly enhanced with respect to $F = 0$. At $F/t^* = 4$, the in-gap WS bands are located at $\omega_{\mathrm{WS},\pm,\mp} \approx 0$, thus making states available around $\omega = 0$ that could in principle be filled by the fermionic bath with a negligible cost in energy [53]. However, these states provide the pathway to promote only the electrons belonging to the LHB into the UHB, as will be confirmed by the discussion in Sec. IV B. In particular, $N_e(\omega)$ shows that the overlapping WS peaks $\omega_{\mathrm{WS},\pm,\mp}$ and the UHB are now considerably occupied. However, the occupation of the former is due to the LHB of one site entering the gap of a neighboring site, while the latter originates from the meeting of the LHB and UHB of sites lying two lattice spacings apart [2,18]. The situation for $F \gtrsim U/2$ can be understood by considering the case $F = 5.6t^* \approx 2U/3$ in Fig. 3(c): here the WS sidebands occur at $\omega_{\mathrm{WS},\pm,\mp} \approx \mp 1.4t^*$ and the spectral occupation $N_e(\omega)$ shows that only $\omega_{\mathrm{WS},\pm,\mp} \approx 1.4t^*$ is considerably occupied. As we will see in Sec. IV A 2, also here the current is enhanced due to charge migration from the LHB to the WS sidebands but it is still smaller than at the *resonance* $F \approx U$. For $F \approx U$ the spectral function shows no WS peaks because of the perfect matching of the lower and upper Hubbard bands. At the same time $N_e(\omega)$ shows that they are almost equally filled [Fig. 3(d)]. We note that this condition is the signature of the fermionic bath draining particles from the UHB back to the LHB [14]. A comparison with the case including only phonons as the source of dissipation discussed in Sec. IV B will corroborate this statement.

Second-order WS sidebands at $\omega_{\mathrm{WS2},\pm,\mp 2} = \pm(3U/2) \mp 2F$ can be also observed, confirming the findings in [18]. These faint features, highlighted by black arrows in Fig. 4(a), first move towards one another as the field increases [see the
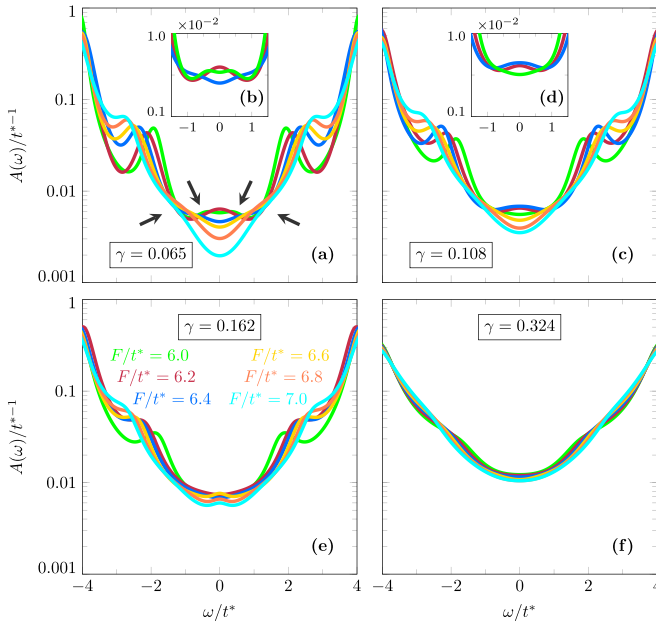
FIG. 4. (a) WS in-gap states at $\omega_{\text{WS},\pm,\mp} = \pm(U/2) \mp F$ in the spectral function $A(\omega)/t^{*-1}$, for various fields F at $\gamma = 0.065$. Black arrows point to the position of $\omega_{\text{WS2},\pm,\mp2} = \pm(3U/2) \mp 2F$, while inset (b) shows the magnified region $\omega/t^* \in [-1.5, 1.5]$ for selected field strengths. (c), (d) Same for $\gamma = 0.108$. (e), (f) WS in-gap states $\omega_{\text{WS},\pm,\mp}$ for $\gamma = 0.162$ and $\gamma = 0.324$. Default parameters are specified at the beginning of Sec. IV.

inset Fig. 4(b) for $F/t^* = \{6.0, 6.2, 6.4\}$] and then run past each other, approaching the main Hubbard bands as the field is further increased. They are associated with adding a particle to a single occupied site (energy $U/2$) with the simultaneous creation of a doublon-holon pair (energy U), accompanied by a tunneling of two particles over one lattice site. However, accounting for second-order processes, these sidebands become relevant at $F \gtrsim U/2$ but are only visible on the logarithmic scale as shown in Figs. 4(a) and 4(b). Also, they are easily washed away by increasing the coupling Γ_e to the fermionic bath, as evidenced in Figs. 4(c) and 4(f). To visualize their faint signature, consider the case of $F = 5.6t^* \approx 2U/3$ shown in Fig. 3(c). Here the WS states $\omega_{\text{WS2},\pm,\mp2} \approx \pm0.8t^*$ do not contribute significantly to the current: as evidenced from $N_e(\omega)$, the net motion of charge carriers mainly involves the transition $\omega_{\text{HB},-} \approx -U/2 \rightarrow \omega_{\text{WS},-,+} \approx -U/2 + 2U/3$, in agreement with previous work [18].

The spectral properties described so far are quite robust against the inclusion of phonons as can be inferred by comparison with [18] which only incorporated dissipation via electrons. We note, however, that increasing Γ_e tends to fill the gap, as can be seen both in the inset Fig. 1(b) as well as in Figs. 4(c)–4(f). This is accompanied by an evident trend to *wash away* the WS satellite peaks. For a given field strength F, a larger Γ_e flattens the states $\omega_{\text{WS2},\pm,\mp2}$ and broadens the subpeaks $\omega_{\text{WS},\pm,\mp}$, accelerating their merging with the Hubbard bands. WS states are then barely visible even on a logarithmic scale as is the case for $\gamma = 0.324$ seen in Fig. 4(f).

Finally, we offer a brief remark on the orientation of the electric field and how it affects the results presented thus far.

We observe that resonances like the one at $F \simeq U/2$, and their meltdown as the field moves off that value, appear to be quite robust; see also the so-called Bloch-Zener islands mentioned in [14] where $\boldsymbol{F} = F\boldsymbol{e}_x$. On the other hand, the fact that neighboring sites do not have isoenergy surfaces may prevent or strongly suppress the dimensional crossover [14,22] at $F \simeq U$ due to the equivalence of all spatial directions.

2. Current, energy, and double occupancy

In the Coulomb gauge, an electron that tunnels through m lattice spacings acquires or loses the potential energy $E_m(F) = mF$. In particular, when the difference is $\Delta E \equiv U - E_m(F) \approx 0$, the current is enhanced due to the resonant creation of doublon-holon pairs which lie m sites apart. However, these resonances are exponentially suppressed by a factor $(t^*/U)^{|m|}$. For instance, Fig. 5(a) shows clear resonances in the steady-state current (25) at $F \approx U/2$ and U, as expected from Sec. IV A 1 [see Figs. 3(b)–3(d)]. In these cases charge migration is due to electrons tunneling from LHB to UHB belonging to sites $|m| = 2$ ($F = U/2$) and $|m| = 1$ ($F = U$) lattice spacings apart. The peak at $F \approx U/3$, on the other hand, is strongly suppressed according to $(t^*/U)^3$ as it accounts for tunneling over $|m| = 3$ lattice sites. In any case, in order to sustain a current, resonant tunneling from a LHB to an UHB m sites away must be followed by relaxation to the LHB. For this reason, the current increases upon increasing γ, as visible in Fig. 5(a). However, the resonances occurring at $F > U/2$ are significantly more sensitive to a larger γ than those at $F < U/2$, the latter being almost unaltered while the former get greatly boosted.

Figure 6 displays the frequency resolved current (26) at field strengths and γ values matching those in Fig. 3 for $A(\omega)$. The largest peaks in $j(\omega)$ marked by dashed lines lie at $\omega_{j,\pm,\mp} = \pm U/2 \mp F/2$: for $F = 3t^*$ they are located at $\omega \approx \pm2.8t^*$ [see Fig. 6(a)]. However, the subpeaks at $\omega/t^* \approx \{\pm0.4, \pm2.2\}$ are not captured by $\omega_{j,\pm,\mp}$. Their origin can be understood with the help of the linear response formula for the tunneling current $j_{\text{tun}}(\omega)$ presented in [18] [see Eq. (20) therein]. In terms of the spectral occupations, it can be written as

$$j_{\text{tun}}(\omega) = \pi t^{*2}[N_e(\omega)N_h(\omega + F) - N_e(\omega + F)N_h(\omega)], \quad (30)$$

where $N_h(\omega) \equiv A(\omega)[1 - F_{\text{neq}}(\omega)]$ is the hole spectral occupation function.

Positive contributions to $j_{\text{tun}}(\omega)$ originate from particles flowing from the filled low-energy states $N_e(\omega)$ to the empty high-energy ones $N_h(\omega + F)$. It is sufficient to analyze the term $N_e(\omega)N_h(\omega + F)$. In particular, we discuss the cases of $F = 3t^*$ and $5.6t^* \approx 2U/3$. For $F = 3t^*$ shown in Fig. 7(a), the maxima of $N_e(\omega)$ and $N_h(\omega + F)$ do not overlap, resulting in a very small contribution to $j_{\text{tun}}(\omega)$ made clear by the scaling factor of $N_e(\omega)N_h(\omega + F)$. The subpeaks at $\omega/t^* \approx \{\pm0.4, \pm2.2\}$ follow as the result of the overlap of $N_e(\omega)$ and $N_h(\omega + F)$. For $F = 5.6t^*$ displayed in Fig. 7(b), the regions having the largest electron and hole occupations are closer and lead to a hump in the current [see Fig. 5(a)]. From these considerations we see that at $F = 8t^*$ in Fig. 6(b) the electrons can now directly fill the vacancies, as evidenced by the single-peak structure of the frequency resolved current
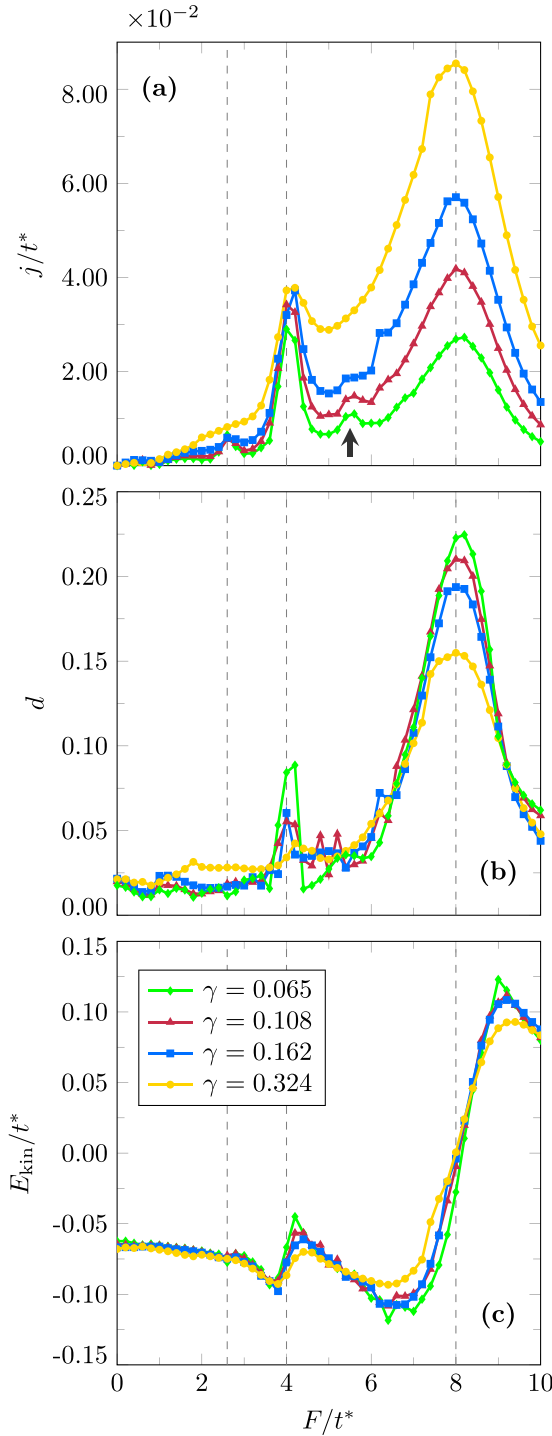
FIG. 5. (a)–(c) Electric field dependence of the steady-state current j, double occupancy d, and kinetic energy E_{kin} for various $\gamma = \Gamma_{\mathrm{e}}/\Gamma_{\mathrm{ph}}$. Dashed vertical lines denote the resonant fields $F = U/3$, $U/2$, and U, while the black arrow highlights the resonance at $F \approx 5.6t^*$. Default parameters are specified at the beginning of Sec. IV.

$j(\omega)$. At the onset of the resonance this effect is balanced by the term $N_{\mathrm{e}}(\omega + F)N_{\mathrm{h}}(\omega)$ since the UHB contains a considerable fraction of particles in the high-energy regions of the spectrum [see Fig. 3(d)].
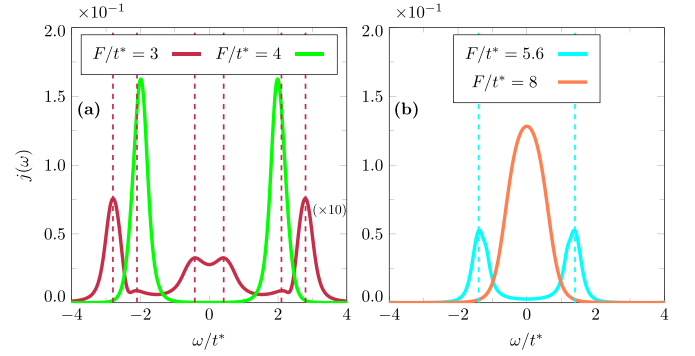
FIG. 6. (a) Frequency resolved current $j(\omega)$ (26) at $F = 3t^*$ and $4t^*$. (b) Same quantity shown for $F = 5.6t^*$ and $8t^*$. Dashed vertical lines mark the maxima discussed in the text. Default parameters are specified at the beginning of Sec. IV.

We emphasize that for $\gamma = 0.065$ the steady-state current at $F \approx U/2$ is slightly larger than the one obtained at $F = U$ [Fig. 5(a)]. This imbalance contrasts with the results in [18] for the same coupling Γ_{e} but agrees qualitatively with those in [16], where a master equation approach employing phononic reservoirs is used as impurity solver. Further details will be given in Sec. IV B.

The double occupation per site is shown in Fig. 5(b). Its main resonances at $F \approx U/2$ and U corroborate the fact that the current is directly related to the creation of doublon-holon pairs. The importance of these processes is evidenced by the resonance at $F \approx 2U/3$ discussed in Sec. IV A, which is clearly visible at $\gamma = 0.065$ and gets smeared out with increasing γ.

In contrast to the trend exhibited by the current j, a stronger fermionic bath suppresses the double occupancy at both $F \approx U/2$ and U. This difference can be explained as follows: as already pointed out [14], a larger γ increases the number of particles that are drained from the UHB and injected back into the LHB. This results in a higher annihilation rate of *doublons*, effectively decreasing the fraction of doubly occupied sites within the lattice.
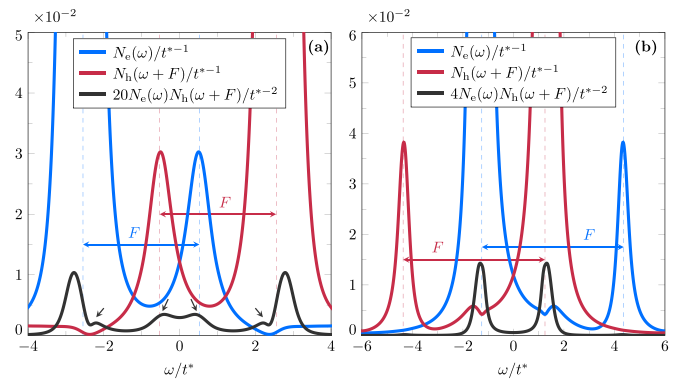

FIG. 7. (a) Electron and hole spectral occupation functions $N_{\mathrm{e}}(\omega)/t^{*-1}$ and $N_{\mathrm{h}}(\omega + F)/t^{*-1}$ and their product at $F = 3t^*$. Black arrows point at the subpeaks discussed in the text [see also Fig. 6(a)]. (b) Same quantities for $F = 5.6t^*$. Here $\gamma = 0.065$ while default parameters are specified at the beginning of Sec. IV.
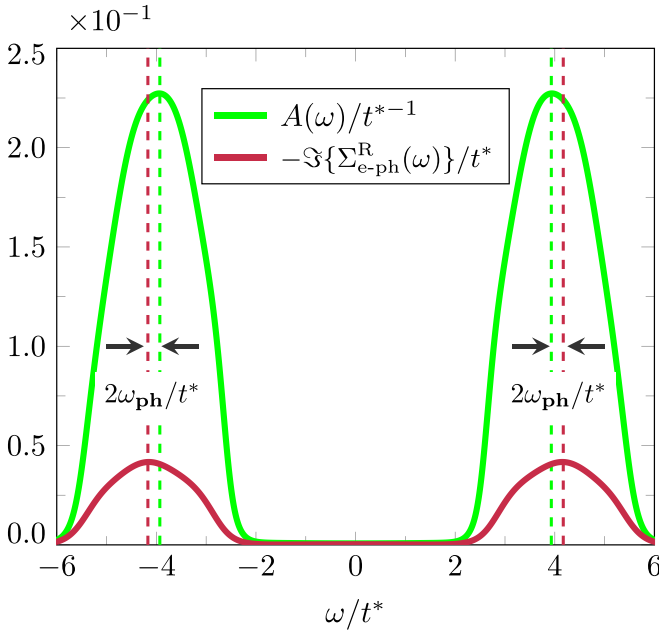
FIG. 8. Electron spectral function $A(\omega)/t^{*-1}$ and e-ph SE $-\mathrm{Im}[\Sigma^{\mathrm{R}}_{\mathrm{e\text{-}ph}}(\omega)]/t^*$ at $F = 0$ for $\gamma = 0$. Dashed vertical lines mark the peaks of A and $-\mathrm{Im}(\Sigma^{\mathrm{R}}_{\mathrm{e\text{-}ph}})$, while arrows highlight the shifts between them. Default parameters are specified at the beginning of Sec. IV.

Since it is related to the creation of a doubly occupied site, knowing d provides information on the interaction energy between the electrons. To fully understand the energy balance, knowledge of the kinetic energy E_{kin} [54] is required as well. Figure 5(c) shows E_{kin} as a function of the applied field. At low fields, E_{kin} decreases as the field is increased independently of γ and in contrast to both j and d. It reaches a local minimum at $F \approx 3.8t^*$, but turns towards a local maximum past $U/2$ at $F/t^* \approx 4.2$–4.4, where d is already showing a downward trend. This behavior signals the energy redistribution within the system. In fact, either the field can enhance the motion of particles, for which an intuitive measure is given by E_{kin}, or the energy can be transferred to particles in a way that allows for a larger number of doubly occupied sites. This interpretation is corroborated by the global maximum of E_{kin} at $F \approx 9t^*$, a field strength where d is suppressed.

B. Dissipation by phonons only

We now discuss the setup including only phonons as dissipation channel, i.e., $\Gamma_{\mathrm{e}} = 0$ [55]. In this case, the e-ph SE $\Sigma_{\mathrm{e\text{-}ph}}$ is strongly determined by $G_{\mathrm{loc}}(\omega)$. In particular a local GF with a gap generates a gapped e-ph SE with the imaginary part of its *retarded* component vanishing in the same frequency region where $\mathrm{Im}(G^{\mathrm{R}}_{\mathrm{loc}})$ vanishes (see Fig. 8). Thus phonons contribute to the dissipation only within a limited frequency window.

1. Spectral properties

In equilibrium at zero field, the spectral function $A(\omega)$ and the e-ph SE $-\mathrm{Im}[\Sigma^{\mathrm{R}}_{\mathrm{e\text{-}ph}}(\omega)]$ are displayed in Fig. 8. $A(\omega)$ features Hubbard bands centered at $\omega_{\mathrm{HB},\pm} = \pm 3.93t^*$ and no *quasiparticle* peak at $\omega = 0$. Similarly, $-\mathrm{Im}[\Sigma^{\mathrm{R}}_{\mathrm{e\text{-}ph}}(\omega)]$
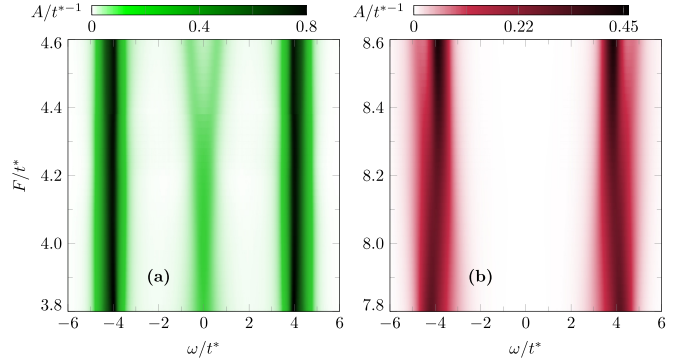

FIG. 9. Color map of the spectral function $A(\omega)/t^{*-1}$ in the accessible regions (a) $F/t^* \in \{3.80, 3.82, \ldots, 4.60\}$ and (b) $F/t^* \in \{7.80, 7.82, \ldots, 8.60\}$. Default parameters are specified at the beginning of Sec. IV.

shows a gap with bands centered at $\omega_{\mathrm{SE},\pm} = \pm 4.17t^*$. The energy shift between the e-ph SE and Hubbard bands amounts to about twice the phonon frequency $|\omega_{\mathrm{HB},\pm} - \omega_{\mathrm{SE},\pm}| = 0.24t^* \approx 2\omega_{\mathrm{ph}}$.

As evidenced by Fig. 8, the e-ph SE $-\mathrm{Im}(\Sigma^{\mathrm{R}}_{\mathrm{e\text{-}ph}})$ is gapped and thus does not provide a dissipation channel over the whole frequency interval. This limits a stable steady-state solution to values of F close to the two main resonances $F/t^* \approx U/2$ and U, the spectra of which are shown in Fig. 9. As in the previous setup, the WS sidebands are present as can be seen in Fig. 9(a): their merging at $F \approx U/2 \approx \omega_{\mathrm{HB},\pm}$ creates the necessary in-gap spectral weight that allows the occupation of the UHB as discussed in Sec. IV A 1.

Figure 10(a) shows a cut of the spectrum displayed in Fig. 9(a) at $F = 4.2t^* \approx \omega_{\mathrm{HB},+} + 2\omega_{\mathrm{ph}} \approx \omega_{\mathrm{SE},+}$, where the current [Fig. 11(a)] reaches its first maximum. We note that the spectral weight and amplitude of the states around $\omega = 0$ are roughly the same as in Fig. 3(b) while the Hubbard bands are narrower, confirming that the fermionic bath provides an overall broadening but has no influence on the transport properties mediated by the in-gap subbands. The corresponding imaginary part of the *retarded* e-ph SE shown in Fig. 10(c) also exhibits a dissipative region around $\omega = 0$, which effectively halves the gap, and facilitates transitions from LHB to UHB.

For field strengths $F \gtrsim 4.6t^*$ the dissipation by phonons is strongly suppressed: this can be explained by the reduction of the in-gap spectral weight at $\omega = 0$ due to the parting WS sidebands as the field is further increased, which is visible in Fig. 9(a). The net effect is that the total spectrum of the in-gap states is no longer sufficient to allow particle decay across the gap [56].

On the other hand, at field strengths crossing the gap, e.g., $F = 2\omega_{\mathrm{HB},+} \approx 7.86t^*$, phonons are expected to dissipate again. In particular, we find that the current increases and reaches its second maximum at $F = 8.42t^* \approx 2(\omega_{\mathrm{HB},+} + 2\omega_{\mathrm{ph}}) \approx 2\omega_{\mathrm{SE},+}$ [Fig. 11(b)]. The corresponding spectral function and e-ph SE profiles are shown in Figs. 10(b) and 10(d). Here the Hubbard bands exhibit a population inversion, as evidenced by the spectral occupation $N_{\mathrm{e}}(\omega)$ and the nonequilibrium distribution function $F_{\mathrm{neq}}(\omega)$. The latter can be approximately described in terms of two effective chemical
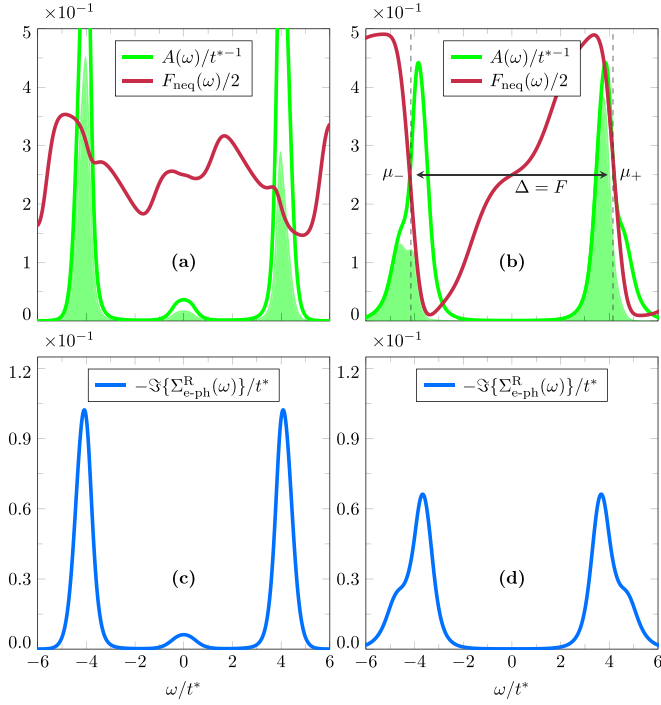
FIG. 10. (a), (c) Spectral function $A(\omega)/t^{*-1}$, spectral occupation $N_e(\omega)/t^{*-1}$ (shaded area), nonequilibrium distribution function $F_{neq}(\omega)$, and e-ph SE $-\mathrm{Im}[\Sigma^R_{e\text{-}ph}(\omega)]/t^*$ at $F/t^* = 4.20$. (b), (d) Same quantities for $F/t^* = 8.42$. The arrow highlights the energy splitting $\Delta = F$ that introduces effective chemical potentials for the Hubbard bands. Default parameters are specified at the beginning of Sec. IV.

potentials $\mu_\pm \approx \omega_{SE,\pm}$ separated by the resonant field, with a larger distribution in the UHB. The steady state is thus characterized by fewer empty states available for transport, resulting in a current, which is almost one order of magnitude smaller than the typical values obtained with the coupling to a fermionic bath. The dissipation mechanism is less effective for phonons alone than in the presence of a fermionic bath. Expanding the nonequilibrium distribution to linear order around the effective chemical potentials as $F_{neq}(\omega \sim \mu_\pm) - 1/2 \approx -(\beta_{eff}/4)(\omega - \mu_\pm)$, one can extract two equal effective temperatures $\beta_{eff} \approx 9/t^*$ [57], while phonons are kept at $\beta = 20/t^*$.

2. Current, energy, and double occupancy

As pointed out in Sec. IV B 1, phonons alone dissipate around the two main resonances $F \approx U/2$ and U. Our results show that the actual peaks in the current are shifted by the phonon frequency and occur at $F = 4.2 \approx \omega_{HB,+} + 2\omega_{ph}$ and $8.42 \approx 2(\omega_{HB,+} + 2\omega_{ph})$ as shown in Figs. 11(a) and 11(b). This implies that the energy range over which phonons affect the system is closely related to their characteristic frequency ω_{ph} (see also Fig. 8).

On the other hand, the slight imbalance in the current at $F \approx U/2$ and U in favor of the former resonance noted for Fig. 5(a) is even stronger in the case of phonon-only dissipation, as evidenced by the suppression of the second resonance peak in Fig. 11(b) (notice the scale).
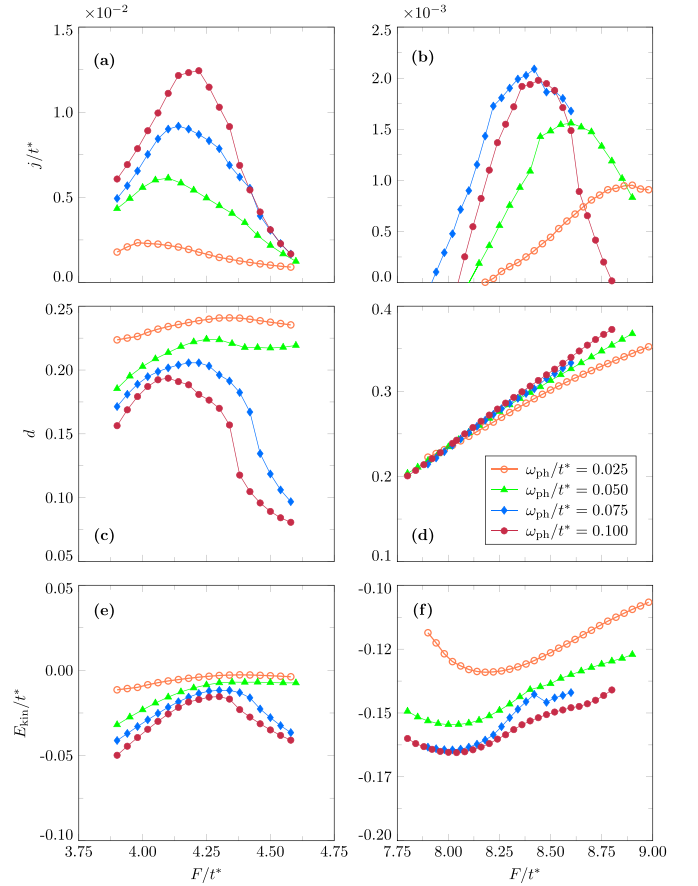

FIG. 11. Electric field dependence of the current (a), (b), double occupation (c), (d), and kinetic energy (e), (f) near the resonances $F/t^* \approx U/2$ and U, for $\omega_{ph}/t^* = \{0.025, 0.050, 0.075, 0.100\}$. The default value of Γ_{ph}/t^* is specified at the beginning of Sec. IV.

For a deeper understanding of the current characteristics, we now focus on the frequency resolved current $j(\omega)$ for field strengths near the resonances mentioned above. Away from the resonant value $F = 4.2t^* \approx \omega_{HB,+} + 2\omega_{ph}$, the frequency resolved current $j(\omega)$ starts to take negative values [see Fig. 12(a)]. This tendency increases at higher field strengths $F \approx 7.8t^*$ [Fig. 12(b)].
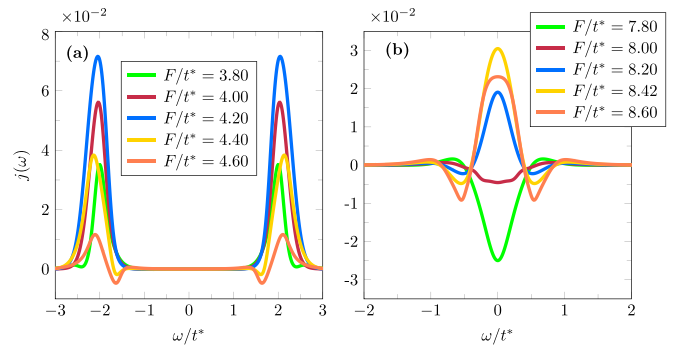

FIG. 12. Frequency resolved current $j(\omega)$ near the resonances at (a) $F/t^* \approx U/2$ and (b) $F/t^* \approx U$. Default parameters are specified at the beginning of Sec. IV.
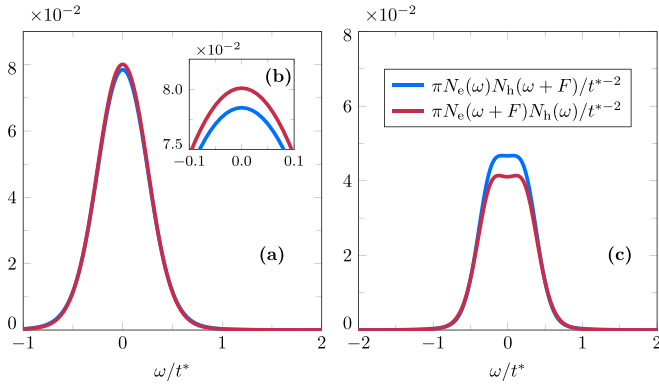
FIG. 13. Forward (blue) and backward (red) flow contributions to the frequency-dependent tunneling current (30). (a), (b) For $F = 7.8t^*$, the backflow overcomes the forwards flow and leads to a negative current. (c) At $F = 8.42t^*$, the forwards flow dominates. Default parameters are specified at the beginning of Sec. IV.

Once again the tunneling formula (30) provides more insight which is illustrated in Fig. 13: when the field is close to the resonance $F \approx U$, particles start to be resonantly promoted from the LHB to the UHB. Lacking the fermionic bath, the accumulation of high-energy carriers within the UHB is due to the backflow $N_e(\omega + F)N_h(\omega)$ which can overcome the forwards flow $N_e(\omega)N_h(\omega + F)$ as shown in Fig. 13(a) (see also [16]). Notably, as the field approaches $F = 8.42t^* \approx 2(\omega_{\text{HB},+} + 2\omega_{\text{ph}})$, the contribution $N_e(\omega)N_h(\omega + F)$ is

sufficiently large to ensure a positive current as seen in Figs. 11(b), 12(b), and 13(b) despite the large number of high-energy occupied states in the UHB visible in Fig. 10(b).

The double occupation per site and the kinetic energy around the two main resonances are shown in Figs. 11(c)–11(f). At $F \approx U/2$ [Figs. 11(c) and 11(e)], both d and E_{kin} follow the same behavior of j. Specifically, they display an ascending phase followed by a downturn. Their maxima are slightly shifted from each other, in agreement with the discussion in Sec. IV A 2. More interesting is the behavior near $F \approx U$ [Figs. 11(d) and 11(f)]. There, the double occupation d increases linearly as a function of F while the kinetic energy E_{kin} first reaches a minimum and then starts to increase as well. The linear increase of the double occupation signals resonant driving and the lack of fermion baths which no longer drain the UHB and inject the particles back in the LHB. For the kinetic energy, the depletion of particles in the LHB implies that less energy can be gained by accelerating particles. In summary, more energy is used to overcome the interaction energy than to increase the kinetic energy. We also note that, while in the case of fermionic baths d never exceeded its *uncorrelated* value $d_{\text{uncorr}} = 0.25$, in the case of only phonons d can increase beyond this value, confirming the accumulation of high-energy doublons seen in Fig. 10(b).

We now investigate how the current depends on the characteristic phonon frequency ω_{ph}. The first resonance sensitively depends on ω_{ph} as can be seen in Fig. 11(a). Its maximum is shifted to $F \approx \omega_{\text{HB},+} + 2\omega_{\text{ph}}$, as already noted in

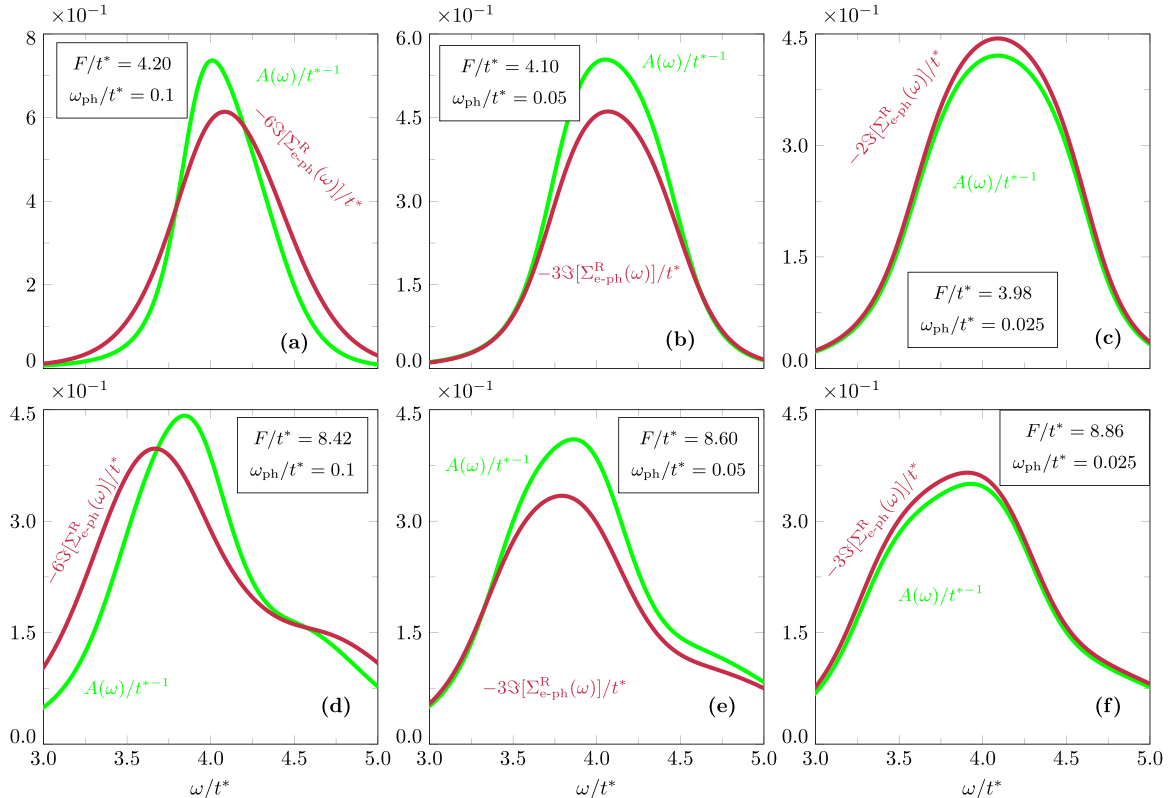FIG. 14. (a), (d) Spectral function $A(\omega)/t^{*-1}$ and e-ph SE $-\text{Im}[\Sigma^R_{\text{e-ph}}(\omega)]/t^*$ displayed for $\omega_{\text{ph}}/t^* = 0.1$ at field strengths which correspond to the current maxima in Figs. 11(a) and 11(b). The same quantities are shown for (b), (e) $\omega_{\text{ph}}/t^* = 0.05$ and (c), (f) $\omega_{\text{ph}}/t^* = 0.025$. Default parameters are specified at the beginning of Sec. IV.

Sec. IV B 1. Also, j grows linearly upon increasing ω_{ph} at this field strength. Considering the current at $F \approx U/2$, the difference between our setup with electronic baths and phonons at $\gamma = 0.065$ discussed in Sec. IV A and the one presented in [18] amounts to the value obtained in the phonon-only setup shown in Fig. 11(a) for $\omega_{ph}/t^* = 0.1$.

The peak at $F \approx U$ displayed in Fig. 11(b) behaves partly different. While the height of the maximum also increases with ω_{ph}, the resonance moves to lower electric fields as the cutoff frequency is increased. This behavior can be explained using Fig. 14, which shows the spectral function and e-ph SE for the peak electric fields belonging to the different cutoff frequencies of Fig. 11. First notice that in the first row [Figs. 14(a)–14(c)] belonging to $F \approx U/2$ the e-ph SE shares the same support as the spectral function. In contrast to this, in the second row [Figs. 14(d)–14(f)] belonging to $F \approx U$, a larger cutoff frequency $\omega_{ph}/t^* = 0.1$ shifts the e-ph SE closer to the gap. This may be due to the increasing ω_{ph} broadening the phonon spectral function $A_{ph}(\omega)$ which thus also broadens the e-ph SE. The broader e-ph SE provides the necessary spectral weight for particle relaxation across the gap, in agreement with the discussion in Sec. IV B 1. In summary the resonance in the current at $F \approx U/2$ is determined by the peak positions of the LHB and UHB which appear to be pinned by the peaks of the e-ph SE as discussed for Fig. 8. Here, the peak positions are decisive, since the particles move via spectral weight located around $\omega = 0$ [see Figs. 10(a) and 10(c)]. For the resonance at $F \approx U$, the spectral weight at both gap edges and thus the extent of the spectral function into the gap are relevant. Here the broadening effect of ω_{ph} seems to determine the resonant electric field.

V. CONCLUSIONS

We investigated the single-particle spectrum and the current characteristics of a Mott insulating system under the action of a strong dc electric field. In this paper we highlighted the effects of acoustic phonons as a dominant mechanism for providing dissipation, thus enabling a stationary dc current, in contrast to fermionic baths adopted in previous work [2,13,14,18].

Starting with the case of both phonons and weakly coupled fermionic baths, we observe the occurrence of in-gap states and transport resonances associated with Wannier-Stark sidebands similar to previous work [14,18]. In the case of phonons as the only source of dissipation, we find them to be much less effective, meaning that a steady-state solution is achieved only for electric fields close to the resonances. In these regions, we find a direct correlation between the resonances' location and the phonon characteristic frequency. In addition, we observe a strong population shift to higher bands around the resonances and in particular a population inversion at large fields which can be described in terms of two separate chemical potentials for the LHB and the UHB. These effects are not observed for the mixed fermion-phonon dissipation mechanism due to the constant drain and emission of carriers by the fermionic baths. When phonons are the *only* dissipation mechanism, the current in the metallic phase is almost one order of magnitude smaller than the typical values obtained by coupling to the fermionic bath.

Employing the so-called self-consistent Migdal approximation which allows phonons to heat up via backaction from electrons is expected to display an even less effective dissipation characterized by a further reduction of the current due to hot-phonon effects at the onset of the metallic phase. However, acoustic phonons could still be able to dissipate to some extent because of their finite, albeit small, bandwidth. This aspect will be investigated in a future work.

As pointed out in previous works [15,18,58], experimentally the quasistationary situation considered here cannot be induced by a regular dc field, since it would have to be far too strong and destroy the material. Following the reasoning in [18], high electric field amplitudes $F \approx 1\,\mathrm{V/Å}$ corresponding to our units are available in the terahertz regime from few cycle pulses which are used for high harmonic generation from solids [59,60]. They argue that below driving frequencies of the order of a few hundred terahertz some of the spectral features could be safely described by a *quasi-dc* setup. To our knowledge, unfortunately such WS excitations have not been observed so far.

APPENDIX A: THE d-DIMENSIONAL CURRENT AND KINETIC ENERGY

We start from the *equal-time* GF $G_{\boldsymbol{k}}^<(t,t) \equiv G_{\boldsymbol{k}}^<(t_{av}, t_{rel} = 0)$, which follows from Eq. (8) as

$$G_{\boldsymbol{k}}^<(t_{av}, t_{rel} = 0) = \sum_{l'=-\infty}^{+\infty} \int_{-\infty}^{+\infty} \frac{d\omega}{2\pi}\, G_{l'}^<(\omega, \boldsymbol{k}) e^{-il\Omega t_{av}}. \quad \text{(A1)}$$

Following [29], the lth Wigner component of Eq. (23) is given by $j_l(\Omega) = \int_{-\frac{\tau}{2}}^{\frac{\tau}{2}} \frac{dt_{av}}{\tau}\, e^{il\Omega t_{av}} j(t_{av})$ which leads combined with Eq. (A1) to

$$j_l(\omega) = 2i \sum_{l'=-\infty}^{+\infty} \sum_{\boldsymbol{k}} [\boldsymbol{e}_0 \cdot \nabla_{\boldsymbol{k}}(\varepsilon_{\boldsymbol{k}})_{l-l'}] G_{l'}^<(\omega, \boldsymbol{k}). \quad \text{(A2)}$$

The d-dimensional $\boldsymbol{k}$-space derivative in Eq. (A2) reads

$$\boldsymbol{e}_0 \cdot \nabla_{\boldsymbol{k}}(\epsilon_{\boldsymbol{k}})_{l-l'} = \sum_{n=1}^{d} \frac{\partial}{\partial k_n}(\epsilon_{\boldsymbol{k}})_{l-l'}$$

$$= \sum_{n=1}^{d} \left[\frac{\partial \epsilon}{\partial k_n} \frac{\partial (\epsilon_{\boldsymbol{k}})_{l-l'}}{\partial \epsilon} + \frac{\partial \bar{\epsilon}}{\partial k_n} \frac{\partial (\epsilon_{\boldsymbol{k}})_{l-l'}}{\partial \bar{\epsilon}} \right], \quad \text{(A3)}$$

where by means of the Floquet dispersion relation in Eq. (14) one finds

$$\frac{\partial (\epsilon_{\boldsymbol{k}})_{l-l'}}{\partial \epsilon} = \frac{1}{2}[\delta_{l-l',1} + \delta_{l-l',-1}],$$

$$\frac{\partial (\epsilon_{\boldsymbol{k}})_{l-l'}}{\partial \bar{\epsilon}} = \frac{i}{2}[\delta_{l-l',1} - \delta_{l-l',-1}]. \quad \text{(A4)}$$

Since Eq. (A4) does not depend on the index n, one can make use of the explicit form of ϵ and $\bar{\epsilon}$ in Eq. (4) and write

$$\sum_{n=1}^{d} \frac{\partial \epsilon}{\partial k_n} = -\bar{\epsilon},$$

$$\sum_{n=1}^{d} \frac{\partial \bar{\epsilon}}{\partial k_n} = \epsilon. \qquad (A5)$$

By inserting Eqs. (A4) and (A5) into Eq. (A3) while recalling that the sum over $\boldsymbol{k}$ can be performed over $(\epsilon, \bar{\epsilon})$, the current integrand is

$$j_l(\omega) = \int d\epsilon \int d\bar{\epsilon}\, \rho(\epsilon, \bar{\epsilon})$$
$$\times [-(\epsilon + i\bar{\epsilon}) G_{l-1}^{<}(\omega, \epsilon, \bar{\epsilon}) + (\epsilon - i\bar{\epsilon}) G_{l+1}^{<}(\omega, \epsilon, \bar{\epsilon})], \qquad (A6)$$

which can be recast as in Eq. (26) exploiting the symmetry property $(\boldsymbol{G}^{<})^{\dagger} = -\boldsymbol{G}^{<}$ and the Floquet-to-Wigner mapping provided in Eq. (9).

We now summarize the main steps to derive the kinetic energy integrand in Eq. (28). The starting point is the analog of Eq. (A2), i.e.,

$$E_{\mathrm{kin},l}(\omega) = -2i \sum_{l'=-\infty}^{+\infty} \sum_{\boldsymbol{k}} (\varepsilon_{\boldsymbol{k}})_{l-l'} G_{l'}^{<}(\omega, \boldsymbol{k}) \qquad (A7)$$

expressing the lth Wigner component of the kinetic energy integrand. As in the previous case, by inserting the Floquet dispersion relation (14) in Eq. (A7) and making use of the JDOS, we get

$$E_{\mathrm{kin},l}(\omega) = \int d\epsilon \int d\bar{\epsilon}\, \rho(\epsilon, \bar{\epsilon})[(\bar{\epsilon} - i\epsilon)$$
$$\times G_{l-1}^{<}(\omega, \epsilon, \bar{\epsilon}) - (\bar{\epsilon} + i\epsilon) G_{l+1}^{<}(\omega, \epsilon, \bar{\epsilon})], \qquad (A8)$$

which is equivalent to Eq. (28) as it can be proven by using the same properties mentioned above.

APPENDIX B: REAL-TIME KELDYSH COMPONENTS OF THE ELECTRON-PHONON SE

The Keldysh components of the e-ph SE in Eq. (16) are explicitly derived by means of the *Langreth rules* [61] and read

$$\Sigma_{\mathrm{e\text{-}ph}}^{R}(t, t') = ig^2 \big[G^{R}(t, t') D_{\mathrm{ph}}^{>}(t, t') + G^{<}(t, t') D_{\mathrm{ph}}^{R}(t, t') \big],$$

$$\Sigma_{\mathrm{e\text{-}ph}}^{K}(t, t') = ig^2 \{ G^{K}(t, t') D_{\mathrm{ph}}^{>}(t, t')$$
$$+ G^{<}(t, t') [D_{\mathrm{ph}}^{>}(t, t') - D_{\mathrm{ph}}^{<}(t, t')] \}, \qquad (B1)$$
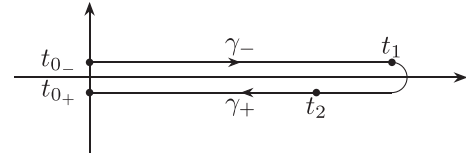

FIG. 15. Keldysh contour $C_\kappa = \gamma_- \cup \gamma_+$ for real-time arguments.

where t and t' lie on the Keldysh contour C_κ shown in Fig. 15.

APPENDIX C: PHONON SPECTRAL FUNCTION

The dispersion relation of acoustic phonon branches can be approximated [62] by

$$\omega(\boldsymbol{q}) \approx v_{\mathrm{s}} |\boldsymbol{q}| \qquad (C1)$$

for reciprocal lattice vectors $\boldsymbol{q}$ satisfying $|\boldsymbol{q}| a \ll 1$, where v_{s} is the characteristic speed of sound of the considered lattice, and a is the lattice spacing. In d dimensions the phonon modes' density of states is

$$D_d(\omega) = \sum_{\boldsymbol{q}} \delta[\omega - \omega(\boldsymbol{q})] = \left(\frac{a}{2\pi}\right)^d \int d^d q\, \delta[\omega - \omega(\boldsymbol{q})]. \qquad (C2)$$

By taking into account $d = \{1, 2, 3\}$ and making use of polar coordinates we find

$$D_1(\omega) = \frac{a}{2\pi} \int_0^{+\infty} d|\boldsymbol{q}|\, \delta(\omega - v_{\mathrm{s}}|\boldsymbol{q}|),$$

$$D_2(\omega) = \left(\frac{a}{2\pi}\right)^2 2\pi \int_0^{+\infty} d|\boldsymbol{q}|\, |\boldsymbol{q}| \delta(\omega - v_{\mathrm{s}}|\boldsymbol{q}|), \qquad (C3)$$

$$D_3(\omega) = \left(\frac{a}{2\pi}\right)^3 4\pi \int_0^{+\infty} d|\boldsymbol{q}|\, |\boldsymbol{q}|^2 \delta(\omega - v_{\mathrm{s}}|\boldsymbol{q}|).$$

Recalling that $\delta(\omega - v_{\mathrm{s}}|\boldsymbol{q}|) = \frac{1}{v_{\mathrm{s}}}\delta(|\boldsymbol{q}| - \omega/v_{\mathrm{s}})$, we then get

$$D_1(\omega) = \frac{a}{2\pi} \frac{1}{2v_{\mathrm{s}}},$$

$$D_2(\omega) = \frac{a^2}{\pi} \frac{\omega}{4v_{\mathrm{s}}^2}, \qquad (C4)$$

$$D_3(\omega) = \frac{a^3}{2\pi^2} \frac{\omega^2}{2v_{\mathrm{s}}^3}.$$

A rough estimate for v_{s} can be obtained as $v_{\mathrm{s}} \approx \omega_{\mathrm{ph}} a$. Here ω_{ph} is the characteristic frequency for which the phonon modes' dispersion relation is still linear, i.e., $\omega_{\mathrm{ph}} = \omega(\boldsymbol{q}_{\mathrm{max}})$. Accordingly $\boldsymbol{q}_{\mathrm{max}}$ is the maximal value the reciprocal lattice vector can take for Eq. (C1) to be fulfilled.

[1] E. Janod, J. Tranchant, B. Corraze, M. Querré, P. Stoliar, M. Rozenberg, T. Cren, D. Roditchev, V. T. Phuoc, M.-P. Besland, and L. Cario, Adv. Funct. Mater. **25**, 6287 (2015).

[2] J. Li, C. Aron, G. Kotliar, and J. E. Han, Phys. Rev. Lett. **114**, 226403 (2015).

[3] J. E. Han, J. Li, C. Aron, and G. Kotliar, Phys. Rev. B **98**, 035145 (2018).

[4] J. E. Han, C. Aron, J.-H. Han, K.-S. Kim, I. Mansaray, M. Randle, and J. P. Bird, arXiv:2205.04396.

[5] P. Stoliar, L. Cario, E. Janod, B. Corraze, C. Guillot-Deudon, S. Salmon-Bourmand, V. Guiot, J. Tranchant, and M. Rozenberg, Adv. Mater. **25**, 3222 (2013).

[6] J. Li, C. Aron, G. Kotliar, and J. E. Han, Nano Lett. **17**, 2994 (2017).

[7] C. Zener and R. H. Fowler, Proc. R. Soc. A **145**, 523 (1934).

[8] T. Oka, R. Arita, and H. Aoki, Phys. Rev. Lett. **91**, 066406 (2003).

[9] T. Oka and H. Aoki, Phys. Rev. Lett. **95**, 137601 (2005).

[10] J. K. Freericks, Phys. Rev. B **77**, 075109 (2008).

[11] A. V. Joura, J. K. Freericks, and T. Pruschke, Phys. Rev. Lett. **101**, 196401 (2008).

[12] M. Eckstein, T. Oka, and P. Werner, Phys. Rev. Lett. **105**, 146404 (2010).

[13] A. Amaricci, C. Weber, M. Capone, and G. Kotliar, Phys. Rev. B **86**, 085110 (2012).

[14] C. Aron, Phys. Rev. B **86**, 085127 (2012).

[15] M. Eckstein and P. Werner, Phys. Rev. B **88**, 075135 (2013).

[16] W.-R. Lee and K. Park, Phys. Rev. B **89**, 205126 (2014).

[17] G. Mazza, A. Amaricci, M. Capone, and M. Fabrizio, Phys. Rev. B **91**, 195124 (2015).

[18] Y. Murakami and P. Werner, Phys. Rev. B **98**, 075102 (2018).

[19] N. Tsuji, T. Oka, and H. Aoki, Phys. Rev. Lett. **103**, 047403 (2009).

[20] J. E. Han, Phys. Rev. B **87**, 085119 (2013).

[21] J. E. Han and J. Li, Phys. Rev. B **88**, 075113 (2013).

[22] C. Aron, G. Kotliar, and C. Weber, Phys. Rev. Lett. **108**, 086401 (2012).

[23] For our purposes, a nonequilibrium steady state is *unstable* if *either* the DMFT loop does not converge *or* convergence is achieved but the observables (current, double occupation, kinetic energy) display very rapid and large (in magnitude) oscillations as a function of adjacent values of the applied electric field.

[24] E. Arrigoni, M. Knap, and W. von der Linden, Phys. Rev. Lett. **110**, 086403 (2013).

[25] A. Dorda, M. Nuss, W. von der Linden, and E. Arrigoni, Phys. Rev. B **89**, 165105 (2014).

[26] A. Dorda, M. Ganahl, H. G. Evertz, W. von der Linden, and E. Arrigoni, Phys. Rev. B **92**, 125145 (2015).

[27] I. Titvinidze, A. Dorda, W. von der Linden, and E. Arrigoni, Phys. Rev. B **92**, 245125 (2015).

[28] M. E. Sorantin, A. Dorda, K. Held, and E. Arrigoni, Phys. Rev. B **97**, 115113 (2018).

[29] N. Tsuji, T. Oka, and H. Aoki, Phys. Rev. B **78**, 235124 (2008).

[30] P. Schmidt and H. Monien, arXiv:cond-mat/0202046.

[31] R. Peierls, Z. Phys. **80**, 763 (1933).

[32] Phonon mixing between the branches is neglected in the spirit of the DMFT approximation and justified by the fact that we are only interested in the properties of the phonons as heat reservoirs.

[33] J. Neumayer, E. Arrigoni, M. Aichhorn, and W. von der Linden, Phys. Rev. B **92**, 125149 (2015).

[34] It should be noted that in the case of the dc field considered here, the system is time independent and so is its GF. Since we choose to work within the temporal gauge, we stick to the Floquet formalism for periodically driven systems, thus we keep using expressions like "characteristic period" and "frequency."

[35] J. Schwinger, J. Math. Phys. **2**, 407 (1961).

[36] L. V. Keldysh, Zh. Eksp. Theor. Fiz. **47**, 1515 (1965) [Sov. Phys. JETP **20**, 1018 (1965)].

[37] J. Rammer and H. Smith, Rev. Mod. Phys. **58**, 323 (1986).

[38] H. Haug and A.-P. Jauho, *Quantum Kinetics in Transport and Optics of Semiconductors* (Springer-Verlag, Heidelberg, 1998).

[39] H. Aoki, N. Tsuji, M. Eckstein, M. Kollar, T. Oka, and P. Werner, Rev. Mod. Phys. **86**, 779 (2014).

[40] Feedback effects from electrons onto phonons are neglected within the *non-self-consistent* version of the Migdal approximation employed in this paper. Thus phonons cannot heat up.

[41] A. Picano, J. Li, and M. Eckstein, Phys. Rev. B **104**, 085108 (2021).

[42] W. Metzner and D. Vollhardt, Phys. Rev. Lett. **62**, 324 (1989).

[43] A. Georges and G. Kotliar, Phys. Rev. B **45**, 6479 (1992).

[44] A. Georges, G. Kotliar, W. Krauth, and M. J. Rozenberg, Rev. Mod. Phys. **68**, 13 (1996).

[45] A. Dorda, M. Sorantin, W. von der Linden, and E. Arrigoni, New J. Phys. **19**, 063005 (2017).

[46] Notice that the accuracy achieved for a certain N_B with AMEA roughly corresponds to the accuracy obtained with a conventional exact-diagonalization impurity solver with more than twice the number of bath sites. This comparison can be done only in equilibrium. For a nonequilibrium steady state a conventional exact diagonalization approach is not possible.

[47] Note that Γ_{ph} cannot be used to infer the phonon relaxation time as $\tau_{ph}^{-1} \sim \Gamma_{ph}$. In fact, such information is encoded in $\text{Im}(\Sigma_{e\text{-ph}}^R)$ rather than in A_{ph}. For this reason one should choose $\Gamma_{ph} = -2\text{Im}[\Sigma_{e\text{-ph}}^R(\omega^*)]$, with ω^* some significant frequency. However, given the strong dependence of the e-ph SE on both the applied field and frequency [see Figs. 8, 10(c), and 10(d)], there is no unique choice of ω^*, which is why we resort to Eq. (29).

[48] We point out that in the sense specified in [23], the smallest coupling Γ_e that ensures convergence over the whole range $F/t^* \in [0, 10]$ equals $\Gamma_e/t^* = 0.065$, for the parameter setup addressed in this paper.

[49] Phonon-only dissipation does not always provide a stable steady state in the sense of [23]. To address the case $\Gamma_e = 0$ at the two main resonances, we initialize our DMFT runs with the converged SEs of the smallest Γ_e employed in Sec. IV A, i.e., $\Gamma_e/t^* = 0.065$ (see also [48]). The electric field strength for this setup is then varied with increments of $\delta F/t^* = 0.02$ around $F \simeq U/2$ and U.

[50] The bandwidths refer to the full width at half maximum.

[51] J. H. Davies and J. W. Wilkins, Phys. Rev. B **38**, 1667 (1988).

[52] V. Turkowski and J. K. Freericks, Phys. Rev. B **71**, 085104 (2005).

[53] Due to the presence of the electric field, there is no true overall Fermi energy. This should be seen as the local one.

[54] We recall that in a simple tight-binding model the kinetic energy starts at negative values.

[55] Upon removal of the fermionic bath one no longer can explicitly fix the chemical potential of the system. In our setup it is implicitly set by enforcing particle-hole symmetry and using the procedure in [49].

[56] Note that as the overall magnitude of the in-gap spectrum diminishes, so does $\text{Im}[\Sigma_{e\text{-ph}}^R]$. Relaxations of high-energy carriers through the gap are only possible if the spectral weight of the

e-ph SE is not too small [see the discussion in Sec. IV A 1 and Fig. 3(b)].

[57] Due to particle-hole symmetry, the two temperatures coincide.

[58] V. Apalkov and M. I. Stockman, Phys. Rev. B **86**, 165118 (2012).

[59] S. Ghimire, A. D. DiChiara, E. Sistrunk, P. Agostini, L. F. DiMauro, and D. A. Reis, Nat. Phys. **7**, 138 (2011).

[60] S. Ghimire and D. A. Reis, Nat. Phys. **15**, 10 (2019).

[61] G. Stefanucci and R. van Leeuwen, *Nonequilibrium Many-Body Theory of Quantum Systems: A Modern Introduction* (Cambridge University, Cambridge, England, 2013).

[62] G. Grosso and G. P. Parravicini, *Solid State Physics* (Academic, New York, 2014).